Interpenetration of fractal clusters drives elasticity in colloidal gels formed upon flow cessation

Noémie Dagès,[a] Louis V. Bouthier, [b] Lauren Matthews, [c] Sébastien Manneville,[a] Thibaut Divoux, [a] Arnaud Poulesquen[d] and Thomas Gibaud [*a]

Colloidal gels are out-of-equilibrium soft solids composed of attractive Brownian particles that form a space-spanning network at low volume fractions. The elastic properties of these systems result from the network microstructure, which is very sensitive to shear history. Here, we take advantage of such sensitivity to tune the viscoelastic properties of a colloidal gel made of carbon black nanoparticles. Starting from a fluidized state at an applied shear rate $\dot{\gamma}_0$, we use an abrupt flow cessation to trigger a liquid-to-solid transition. We observe that the resulting gel is all the more elastic when the shear rate $\dot{\gamma}_0$ is low and that the viscoelastic spectra can be mapped on a master curve. Moreover, coupling rheometry to small angle X-ray scattering allows us to show that the gel microstructure is different from gels solely formed by thermal agitation where only two length scales are observed: the dimension of the colloidal and the dimension of the fractal aggregates. Competition between shear and thermal energy leads to gels with three characteristic length scales. Such gels structure in a percolated network of fractal clusters that interpenetrate each other. Experiments on gels prepared with various shear histories reveal that cluster interpenetration increases with decreasing values of the shear rate $\dot{\gamma}_0$ applied before flow cessation. These observations strongly suggest that cluster interpenetration drives the gel elasticity, which we confirm using a structural model. Our results, which are in stark contrast to previous literature, where gel elasticity was either linked to cluster connectivity or to bending modes, highlight a novel local parameter controlling the macroscopic viscoelastic properties of colloidal gels.

1 Introduction

Colloidal gels are out-of-equilibrium amorphous soft solids composed of attractive Brownian particles that aggregate to form a space-spanning network at low concentrations.[1] These viscoelastic materials are ubiquitous both in nature and in industrial applications as diverse as flow batteries, food products and cementitious materials.[2–5] The scenario underlying their formation, namely the sol–gel transition, governs the vast majority of their structural and mechanical properties. In practice, Brownian motion is the driving force that allows colloids to encounter each other, whereas the colloid concentration ϕ and the interaction potential U set up the aggregation path and the final gel properties.[6,7] In the limit of low concentrations and high interparticle attraction strength, diffusion-limited or reaction-limited cluster aggregation take place and

lead to the formation of fractal gels[8,9] characterised by two length scales, the particle radius r_0 and the cluster size ξ_c of fractal dimension d_f. At intermediate volume fractions and for moderate attraction strength, the sol–gel transition corresponds to an arrested phase separation.[10–12] In the former situation, the gel mechanical properties are captured by fractal scaling,[13,14] whereas in the latter case, the gel properties are set by the connectivity of glassy clusters[15,16] or by the stretching and bending rigidity of the glassy network.[17]

Because colloidal gels are out-of-equilibrium, additional parameters play a key role in controlling their properties. External fields that act on the colloid dynamics and compete with Brownian motion may disrupt the direct correspondence between the gel properties and their coordinates (ϕ, U) in the state diagram, leading to gels with a broad variety of structural and mechanical properties from a single colloidal dispersion. Indeed, the energy landscape of suspensions of attractive colloids is complex and strewn with multiple local minima (Fig. 1). Some of those minima are only accessible with an additional input of energy, larger than the thermal energy k_BT. This is precisely the role of external stimuli, leading gelation into local minima inaccessible *via* Brownian motion. Therefore, the properties of multiple metastable colloidal gels are a

[a] Univ Lyon, Ens de Lyon, Univ Claude Bernard, CNRS, Laboratoire de Physique, F69342 Lyon, France. E-mail: thomas.gibaud@ens-lyon.fr

[b] Groupe CFL, CEMEF, Mines Paristech, 1 Rue Claude Daunesse, 06904 Sophia Antipolis, France

[c] ESRF – The European Synchrotron, 38043 Grenoble Cedex, France

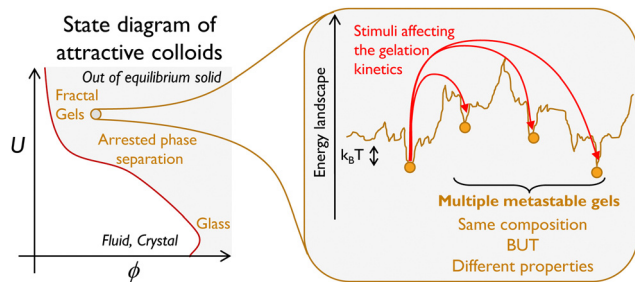[d] CEA, DES, ISEC, DE2D, SEAD, LCBC, Université of Montpellier, Marcoule, France

Fig. 1 Schematic principle of the concept of multiple metastable gels in attractive colloidal dispersions.

function of the external stimuli intensity. At the fundamental level, an external stimulus is ideal for exploring the interplay between the microstructure and mechanics: as the gel originates from the same dispersion, the colloid volume fraction and interactions remain unchanged, while variations in the gel mechanical properties only result from microstructural changes. In practice, different external control parameters such as temperature and external shear have been used as external stimuli. For instance, the microstructure of globular protein gels can be tuned by varying the quench rate during the sol–gel transition: the faster the temperature quenches, the smaller the characteristic length of the gel network.[18] In colloidal gels built from depletion interaction, flow cessation from a shear rate of intensity $\dot{\gamma}_0$ to 0 s^{-1} leads to gels, whose structure and rheology are governed by the intensity of the preshear $\dot{\gamma}_0$: a high preshear $\dot{\gamma}_0$ leads to homogeneous and strong gels whereas a low preshear $\dot{\gamma}_0$ leads to heterogeneous and weak gels.[19] In dispersions of fractal-like particles with attractive interparticle interactions, stress-controlled flow cessation at various cessation rates yields gels whose strength and connectivity increase for an increasing cessation rate.[20]

Despite multiple pieces of evidence that the mechanical properties of colloidal gels can be tuned by an external stimulus, a quantitative correspondence between the gel microstructure and its mechanical properties is still lacking. We have chosen to take up this challenge in the case of mechanical shear applied to particulate colloidal gels with non-covalent interactions for three reasons. First, such colloidal gels can be rejuvenated by shear, *i.e.*, their microstructure can be reconfigured by an external shear of large enough magnitude for a long enough duration, before the gel reforms upon flow cessation.[21,22] Shear rejuvenation allows us to conveniently explore different gelation scenarios on the same sample. Second, it is already well established that shear may interfere with the gelation pathway of particulate colloidal gels, thus giving the opportunity to tune gels in terms of the microstructure,[19,23] connectivity[20] or yield stress.[24] Third, on the application level, such an interplay between shear and gelation is involved in numerous industrial processes, and especially in additive manufacturing where external fields such as an additional shear coupled with 3D printing allow tuning the microstructure and the properties of the printed materials.[25]

In practice, we choose to work with gels of carbon black nanoparticles whose properties can be tuned using shear history.[20,24,26] Here we influence the gelation pathway of these gels as follows:

starting from a fluidized state at an applied shear rate $\dot{\gamma}_0$, an abrupt flow cessation triggers a liquid-to-solid transition. Varying the shear rate intensity $\dot{\gamma}_0$ allows us to generate gels whose viscoelastic properties span over a decade in stress units. Specifically, lower shear intensities yield more elastic gels upon flow cessation, while the viscoelastic spectrum for different $\dot{\gamma}_0$ shows a robust frequency dependence that can be rescaled onto a master curve. Using rheometry coupled to small angle X-ray scattering (SAXS), we further show that the gel microstructure is composed of clusters of size ξ_c and fractal dimension d_f separated by a cluster center to center distance ξ_s. These structural parameters depend on $\dot{\gamma}_0$. More importantly, we show that $\xi_s < \xi_c$ means that adjacent clusters interpenetrate each other. The degree of interpenetration defined by the ξ_c/ξ_s ratio decreases for increasing values of $\dot{\gamma}_0$. The degree of interpenetration is crucial, as it controls the gel elasticity and captures the impact of $\dot{\gamma}_0$ on the gel viscoelastic properties, as confirmed by a fractal scaling model.

The outline of the paper is as follows. We first introduce carbon black gels as well as our experimental toolbox in Section 2. Second, in Section 3, we present our experimental results. We show how shear history allows tuning the gel viscoelastic properties, which can be rescaled onto a master curve. We then establish that the gel structures in fractal clusters interpenetrate each other. Third, in Section 4, after dismissing a superposition principle to account for the scaling of the viscoelastic properties of the gel, we derive a fractal scaling model establishing a direct link between the gel microstructure and the gel network elasticity as a function of the shear rate intensity $\dot{\gamma}_0$ applied before flow cessation.

2 Materials and methods

2.1 Carbon black dispersions

Carbon black (CB) particles are fractal carbonated colloids that result from the partial combustion of hydrocarbon oils.[27–29] These particles are widely used in the industry for mechanical reinforcement or to enhance the electrical conductivity of plastic and rubber materials.[30] Among the large variety of carbon black particles,[26,31–34] we choose to work with Vulcan PF particles (Cabot, density d_{cb} = 2.26 ± 0.03). The density of Vulcan PF particles is d_{cb} = 2.26 ± 0.03 and we estimate their radius of gyration r_g = 35 nm with a 20% polydispersity and their fractal dimension d_{f0} = 2.9 (see Appendix A.1 for details).

When dispersed in mineral oil (RTM17 Mineral Oil Rotational Viscometer Standard, Paragon Scientific, viscosity η = 354 mPa s at T = 20 °C, density d_{bck} = 0.871), CB particles are weakly attractive. The depth U of the interparticle potential depends on the type of CB particles, the solvent, and the presence of a dispersant and falls typically in the range $U \sim 10$–$30 k_B T$.[35,36] At a working weight concentration in CB particles of c_w = 4%, the particles aggregate to form a gel, *i.e.*, a space-spanning network, which behaves as a viscoelastic soft solid. Indeed, at rest, the elastic modulus G' dominates the viscous modulus G'' in the limit of low frequencies, whereas the sample displays a solid-to-liquid transition beyond a critical strain $\gamma_y \sim 10\%$.

Moreover, under steady shear, the flow curve that links the shear stress σ to the shear rate $\dot{\gamma}$ is well fitted by the Herschel–Bulkley model, $\sigma = \sigma_y + K\dot{\gamma}^n$,[37] with a dynamical yield stress $\sigma_y = 4.5$ Pa, a consistency index $K = 1.0$ Pa.s$^{1/0.83}$, and a fluidity index $n = 0.83$ (see Fig. 8 in Appendix A.2).

2.2 Rheology

In the present work, we use a rheometer both to measure the mechanical properties of CB gels and to shape up their microstructures. We carry out our experiments with two stress-controlled rheometers: (i) an MCR301 (Anton Paar) equipped with a rough cone (radius 40 mm, angle 1°) and a smooth bottom plate both made of steel and (ii) a Haake RS6000 (Thermo Scientific) equipped with a Couette geometry composed of concentric polycarbonate cylinders (inner diameter 20 mm, outer diameter 22 mm, and height 40 mm) for rheo-SAXS experiments. Both apparatuses give identical results provided that the shear rate does not exceed 500 s^{-1} in the Couette geometry due to the Taylor–Couette instability.[38]

2.3 Small angle X-ray scattering

The microstructural properties of the carbon black dispersion are investigated using rheo-SAXS measurements carried out on the ID02 beamline at the European Synchrotron Radiation Facility (ESRF, Grenoble, France).[39] The incident X-ray beam of wavelength 0.1 nm is collimated to a vertical size of 50 μm and a horizontal size of 100 μm. The 2D scattering patterns were measured using an Eiger2 4M pixel array detector, and the subsequent data reduction procedure is described elsewhere.[40] The scattering intensity $I(q)$ is obtained by subtracting the two-dimensional scattering patterns of the carbon black gel and the mineral oil. The resulting scattering intensity presented in this article always remained isotropic (see Fig. 14 in Appendix A.7). Therefore, we radially averaged the normalized intensity pattern to obtain one dimensional $I(q)$. Note that measurements were performed in both radial and tangential configurations, and they turn out to be equivalent due to the isotropy of the gel microstructure.

2.4 Rheological protocol

We apply the protocol sketched in Fig. 2, which is divided into two sequences: a flow cessation sequence to shape up the gel
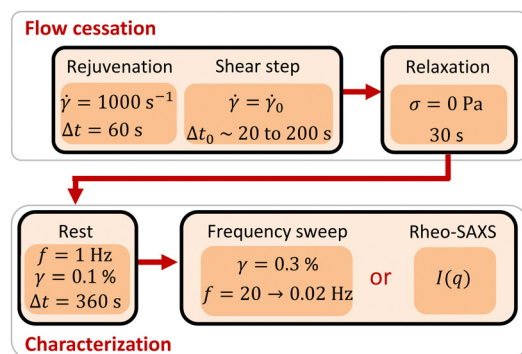
properties followed by a sequence of characterization of the gel mechanical properties inherited from the flow cessation protocol.

In practice, the flow cessation protocol is divided into three steps. First, we carry out a rejuvenation step during which the sample is sheared at $\dot{\gamma} = 1000$ s^{-1} for $\Delta t = 60$ s to erase any shear history that would influence the gel mechanical properties later on. Second, we modify the shear intensity by imposing a quench from $\dot{\gamma} = 1000$ s^{-1} to a constant shear rate $\dot{\gamma}_0 \in [0.1, 1500]$ s^{-1} for a duration $\Delta t_0 \in [20, 200]$ s. Fig. 3(a) shows the stress response $\sigma(t)$ of the CB gel resulting from quenches to various values of $\dot{\gamma}_0$. For high shear rates $\dot{\gamma}_0$, a duration of $\Delta t_0 = 20$ s is sufficient to reach a steady state. However, for $\dot{\gamma}_0 < 10$ s^{-1}, we must impose $\dot{\gamma}_0$ for longer durations, as σ increases significantly, before reaching a maximum and then slowly decreases. The increase of σ at short time scales corresponds to a transient regime necessary for the system to adapt to the new shear rate $\dot{\gamma}_0$[42] (see also Appendix A.2). The slow decrease at longer time scales might be due to some slippage of the dispersion at the walls of the shear cell.[43] Third, we apply a flow cessation by imposing $\sigma = 0$ Pa for 30 s, while recording the shear-rate response $\dot{\gamma}(t)$ as displayed in Fig. 3(b). We observe that $\dot{\gamma}$ decreases to values beneath 10^{-3} s^{-1} within a few
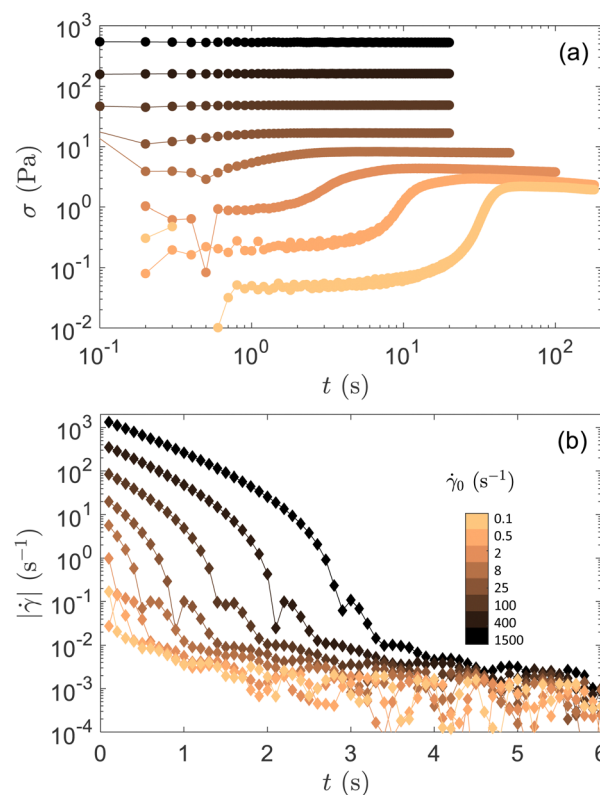

Fig. 3 Flow cessation sequence performed with different values of the shear rate $\dot{\gamma}_0$ in a $c_w = 4\%$ carbon black dispersions. The sequence is composed of two steps: a quench in shear rate from 1000 s^{-1} to $\dot{\gamma}_0$ yielding a stress response $\sigma(t)$ pictured in (a), followed by a complete flow cessation which results in (b) the relaxation of $|\dot{\gamma}|(t)$ when imposing $\sigma = 0$ Pa. In (a and b), colors encode the value of $\dot{\gamma}_0$ ranging from 1500 (black) to 0.1 s^{-1} (yellow), see the legend in (b).

Fig. 2 Experimental protocol: schematic of the flow cessation and characterization sequences.

seconds indicating that the rotor is immobile and that flow cessation is complete. At short time scales, the shear rate decreases exponentially as expected for a simple, viscous fluid. At intermediate timescales, $\dot{\gamma}$ drops faster than exponentially and displays oscillations typical of the viscoelastic ringing observed in soft solids during creep tests.[44–47] This indicates that gels reform within a few seconds.

Finally, the characterization sequence following flow cessation consists in three steps. First, we let the system rest for 360 s, while measuring the elastic G' and viscous G'' modulus using oscillations of small amplitude $\gamma = 0.1\%$ at a frequency $f = 1$ Hz. As shown in Fig. 9 in Appendix A.4, the viscoelastic moduli of the dispersion rapidly reach a regime where aging is weak. Second, we perform a frequency sweep at $\gamma = 0.3\%$ with 10 points per decade for frequencies f ranging from 0.02 to 20 Hz. To gain some insights into the gel microstructure during these two sequences, the entire protocol was carried out in the rheo-SAXS setup for four distinct shear intensities $\dot{\gamma}_0$. The scattered intensity $I(q)$ of the gel obtained after flow cessation is discussed in the next section.

Based on ref. 48, we estimate that throughout the rheological protocol the gel is homogeneously sheared and does not display shear banding. Indeed shear banding may appear in carbon black suspensions. When going from a large to a low value of the shear rate, shear banding only happens below a critical shear rate of $\dot{\gamma}_{SB}$. $\dot{\gamma}_{SB}$ is easily identifiable on the flow curve by a drop of the shear stress σ at low shear rates. From Fig. 8, we determine $\dot{\gamma}_{SB} \sim 0.1$ s^{-1}. This value justifies carrying out preshear of intensity $\dot{\gamma}_0$ no lower than 0.1 s^{-1} to guarantee the homogeneity of the flow profile in the rheometer.

3 Results

3.1 Impact of the shear rate $\dot{\gamma}_0$ on the gel linear viscoelastic spectrum

We first focus on the impact of $\dot{\gamma}_0$ on the linear viscoelastic properties of the gel formed upon flow cessation (see "Frequency sweep" in the characterization sequence sketched in Fig. 2). The gel frequency spectrum is reported in Fig. 4(a) for various values of the shear rate intensity $\dot{\gamma}_0$ spanning over four decades. Overall, we observe that low $\dot{\gamma}_0$ produces more elastic gels. More precisely, whatever the shear rate intensity $\dot{\gamma}_0$, the elastic and viscous moduli are increasing functions of the frequency and cross at a frequency f_c that shifts towards larger values for decreasing $\dot{\gamma}_0$. Moreover, in the limit of low frequencies, all spectra show a plateau in elasticity with $G' > G''$, which confirms the solid-like behavior of the sample, regardless of the shear rate intensity applied prior to flow cessation. The shape of the viscoelastic spectrum is robust and appears merely shifted, which prompts us to construct a master curve from the data in Fig. 4(a). By normalizing each spectrum by the coordinate (f_c, G_c) defined by the crossover of G' and G'', we obtain the master curve reported in Fig. 4(b). This scaling behavior is also clearly visible in the $\tan(\delta) = G''/G'$ representation. Since G' and G'' are scaled by the same factor, building a master curve with $\tan(\delta)$ from different $\dot{\gamma}_0$ only requires to scale the frequency axis as shown in Fig. 10. The asymptotic behavior of the master curve corresponds to a Kelvin–Voigt model (see Appendix A.5) displayed as blue lines in Fig. 4(b). At low frequencies, *i.e.*, $f \ll f_c$, the elastic modulus G' tends towards a plateau value much larger than G'', which is the hallmark of a solid-like behavior at rest. At high frequencies, *i.e.*, $f \gg f_c$, the
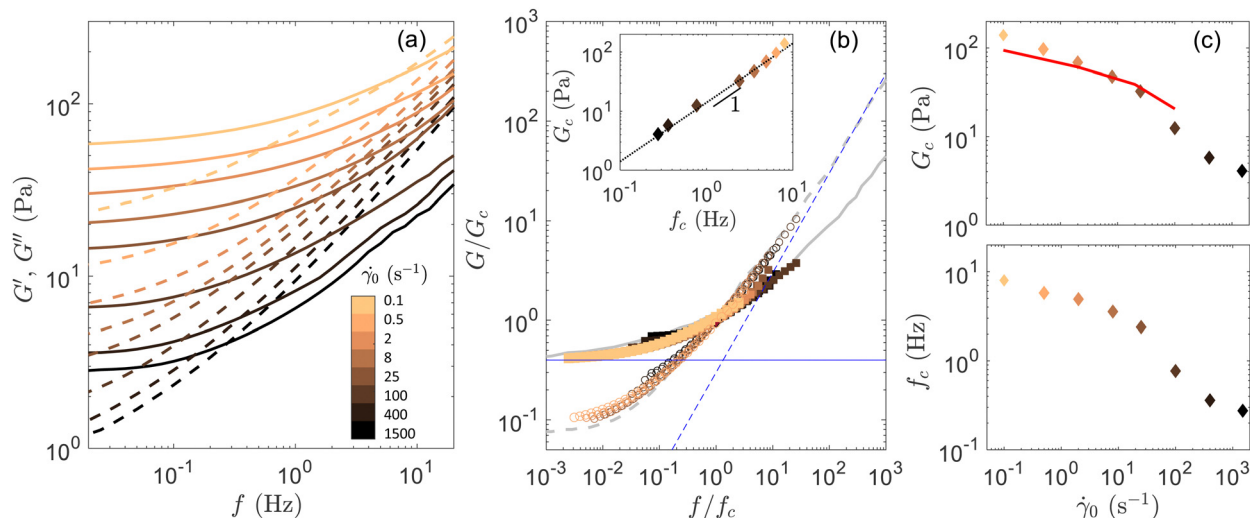

Fig. 4 Impact of the shear rate applied before flow cessation on the gel viscoelasticity. (a) Elastic G' and viscous modulus G'' *vs.* the frequency f in a $c_w = 4\%$ carbon black dispersions. The color codes for the shear rate intensity $\dot{\gamma}_0$ applied before flow cessation. (b) Normalized viscoelastic spectrum: G'/G_c and G''/G_c *vs.* the normalized frequency f/f_c, where G_c and f_c denote, respectively, the modulus and the frequency at which $G' = G''$ in (a). The blue curves correspond to a Kelvin–Voigt model (see Appendix A.5). The grey curves correspond to the master curves obtained for G' (solid line) and G'' (dashed line) by rescaling viscoelastic spectra of CB dispersions in oil for various volume fractions [data were extracted from ref. 41]. Inset: G_c *vs.* f_c. The red dotted line is the best linear fit of the data: $G_c = 14.5 f_c$. (c) Evolution of G_c (top) and f_c (bottom) *vs.* $\dot{\gamma}_0$. The red line is the best fit of the data using eqn (1) and the structural information reported in Fig. 6. The best fit is obtained with a single adjustable parameter, namely the prefactor $G_{CB} = 9$ Pa.

viscous modulus G'' dominates and increases linearly with the frequency and the solvent viscosity η, such that $G'' = 2\pi\eta f$. In this range of frequencies, the variations of G'' correspond to the viscous dissipation due to the thermal fluctuations of the gel network in the background solvent. We note that the master curve can be fully fitted by a fractional Kelvin–Voigt model (see Appendix A.5). Such a master curve is strongly reminiscent of that obtained on fractal gels by varying the particle volume fraction and the interparticle potential.[36,41,49] In contrast, here, the master curve is generated by varying the shear history on a sample of fixed composition. Yet, rescaled data extracted from ref. 41 and obtained with different CB particles suspended in another solvent [see gray curves in Fig. 4(b)] fall remarkably well on our master curve. This suggests that various shear histories allow generating gels, whose microstructure shares some similarity with that generated by varying the colloid volume fraction.

The high sensitivity of CB gels to shear history is encoded in the dependence of the locus of G' and G'' crossing point (f_c, G_c) with $\dot{\gamma}_0$. As shown in Fig. 4(c), both f_c and G_c decrease by almost two orders of magnitude when increasing $\dot{\gamma}_0$ from 0.1 s^{-1} to 1500 s^{-1}. Such influence of shear history is not obvious, which shows a trend similar to that observed in boehmite gels[50] and silica sphere and rods gels[51] but opposite to that reported in depletion gels, where a strong shear yields a more homogeneous and more elastic structure upon flow cessation.[19]

3.2 Influence of the carbon black weight concentration

The rescaling and the master curve introduced in Section 3.1 are robust to changes in the CB weight concentration, from $c_w = 2$ to 8%. For instance, the viscoelastic spectrum of a $c_w = 2\%$ carbon black dispersion obtained with various shear rate $\dot{\gamma}_0$

applied before flow cessation can be rescaled on the same master curve as that displayed in Fig. 4(b) (see Fig. 12 in Appendix A.6). Moreover, for a fixed shear intensity $\dot{\gamma}_0$, the modulus G_c increases as a power law of c_w, $c_w = (c_w/C_1)^\alpha$ with a concentration C_1 and an exponent α that depends on $\dot{\gamma}_0$ [Fig. 5(b)]. While a power-law increase of the gel elasticity for increasing particle weight concentration or volume fraction is classically reported in colloidal gels with an exponent α ranging between 2 and 4.5 depending on the range of the interparticle potential and the nature of the particles,[1,36,52] the sensitivity of α to shear history is a key result of the present study. Here, in Fig. 5(b), we show that α increases for increasing shear rate intensity applied before flow cessation varying between $\alpha \simeq 3$ for $\dot{\gamma}_0 = 0.1$ s^{-1} to surprisingly high values, i.e. $\alpha \simeq 7$ for $\dot{\gamma}_0 = 1500$ s^{-1}. Finally, in Fig. 5(c), we show that G_c follows a master curve driven by a dimensionless concentration and shear rate intensity. Although this dependence remains empirical, this master curve highlights the fact that there are many ways to obtain gels with identical G_c. For instance to get $G_c \simeq 3$ Pa, one can either prepare a gel at $c_w = 4\%$, $\dot{\gamma}_0 = 1500$ s^{-1}; $c_w = 3\%$, $\dot{\gamma}_0 = 100$ s^{-1}; or $c_w = 2\%$, $\dot{\gamma}_0 = 2$ s^{-1}.

To connect these results to the gel microstructure, one can be tempted to combine the power-law exponent α with the scaling theories developed for fractal gels,[13] in order to estimate the cluster fractal dimension d_f. The theory developed in the context of Brownian aggregation distinguishes between two types of networks, depending on the relative value of the elastic constant of the inter-cluster links to that of the cluster. In the case of weak links, $\alpha = 1/(3 - d_f)$, which yields $2.6 < d_f < 2.9$, whereas in the case of strong links, $\alpha = (3 + x)/(3 - d_f)$ with $x < d_f$ the fractal dimension of the gel backbone, which yields $1.5 < d_f < 2.5$ (see Fig. 13 in Appendix A.6). These values motivate an experimental characterization of the gel microstructure, and
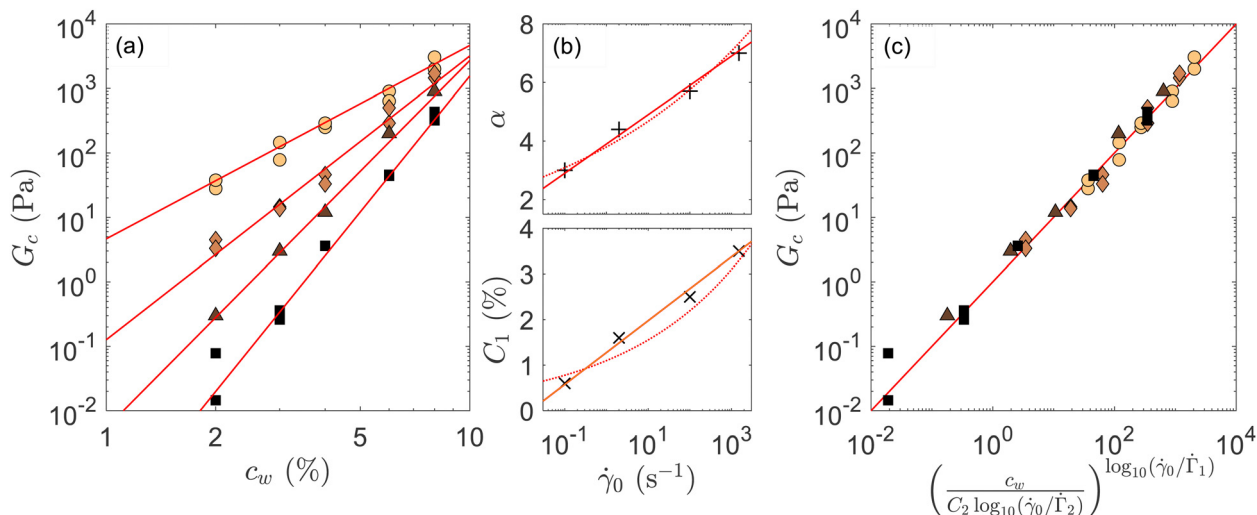

Fig. 5 Influence of the carbon black weight concentration. (a) Evolution of G_c as a function of the weight concentration in carbon black particles c_w for various shear rates applied prior to flow cessation: $\dot{\gamma}_0 = 0.1$ s^{-1} (circle), 2 s^{-1} (diamond), 100 s^{-1} (triangle) and 1500 s^{-1} (square). Red lines are the best power-law fit of the data $G_c = (c_w/C_1)^\alpha$. Both α and C_1 depend on $\dot{\gamma}_0$. (b) α and C_1 vs. the shear rate $\dot{\gamma}_0$. Red lines are the best logarithmic fit of the data: $\alpha = \log_{10}(\dot{\gamma}_0/\dot{\Gamma}_1)$ with $\dot{\Gamma}_1 = 10^{-3.9}$ s^{-1} and $C_1 = C_2 \log_{10}(\dot{\gamma}_0/\dot{\Gamma}_2)$ with $C_2 = 0.7\%$ and $\dot{\Gamma}_2 = 0.015$ s^{-1}. Dotted lines are the best power law fits. (c) Evolution of G_c as a function of the dimensionless concentration and the shear rate.

especially of the cluster fractal dimension to test the relevance of such scaling theories.

3.3 Microstructure of the gel as a function of the shear $\dot{\gamma}_0$ applied before flow cessation

To better understand the interplay between the shear history and the gel microstructural properties, we perform rheo-SAXS experiments using the protocol sketched in Fig. 2. The scattering intensity $I(q)$ measured 360 s after the flow cessation protocol for four different shear rate intensities $\dot{\gamma}_0$ prior to flow cessation is reported in Fig. 6(a), as a function of the wave number q. In all four cases, the scattered intensity $I(q)$ presents similar features. First, $I(q)$ is isotropic, *i.e.*, tangential and radial measurements are equivalent (see Fig. 14 in Appendix A.7). Therefore, the gel displays an isotropic structure at all length scales probed by SAXS, which is why we only report the azimuthally averaged $I(q)$. Second, $I(q)$ presents three characteristic bumps around 0.04, 0.01 and 0.002 nm^{-1} characteristic of three length scales. This structure is atypical. Indeed, in gels driven solely by thermal agitation, $I(q)$ classically displays only two characteristic length scales: the particle size r_0 and the cluster size ξ_c separated by a power-law regime, and the exponent of which is related to the cluster fractal dimension.[53]

Here, we attribute the high-q bump to the CB particles of size r_0, the low-q bump to clusters of size ξ_c and fractal dimension d_f, and the bump at intermediate q to the structural distance ξ_s between the centers of two adjacent clusters. These bumps appear more clearly in the Kratky-like representation $I \cdot q^{d_f}$ reported in Fig. 6(a). In the Kratky-like representation, we used the d_f displayed in Fig. 6(b).

A description of the gel microstructure based on three characteristic length scales is implemented in a modified two-level Beaucage model. In short, the two-level Beaucage model[54,55] accounts for the scattering of clusters of size ξ_c and fractal dimension d_f composed of particles of size r_0. To account for the increase of scattering at ξ_s, we have multiplied the cluster scattering intensity term in the Beaucage model by an *ad hoc* inter-cluster structure factor (see Appendix A.7 for more details). This modified Beaucage model provides an excellent fit for the experimental data obtained for different shear histories [Fig. 6(a)]. Moreover, since the gel weight concentration is identical in the four measurements, the fit parameters r_0, ξ_c, d_f and ξ_s should obey mass conservation. In practice, such a constraint can be expressed at the scale of the unit cell of the gel network, *i.e.*, the minimum structural repeating unit necessary to construct the gel structure defined by the correlation length ξ_s. The number of particles $N = (\xi_c/r_0)^{d_f}$ in a unit cell corresponds to the number of particles in the cluster of size ξ_c and fractal dimension d_f. Based on the values of the fit parameters obtained from adjusting the modified two-level Beaucage model to the SAXS data, we check that, indeed, $\rho = (\xi_c/r_0)^{d_f}/\xi_s^3$ remains constant across the four measurements with $\rho = 7250 \pm 230$ particles per μm^3. This value is also in agreement with the carbon black weight concentration $c_w = 4\%$ (see Fig. 16 in Appendix A.7), which confirms that our analysis of the scattering data is self-consistent.

Fig. 6(b) shows the dependence of the fit parameters ξ_c, ξ_s, and d_f with the shear rate intensity $\dot{\gamma}_0$ applied before flow
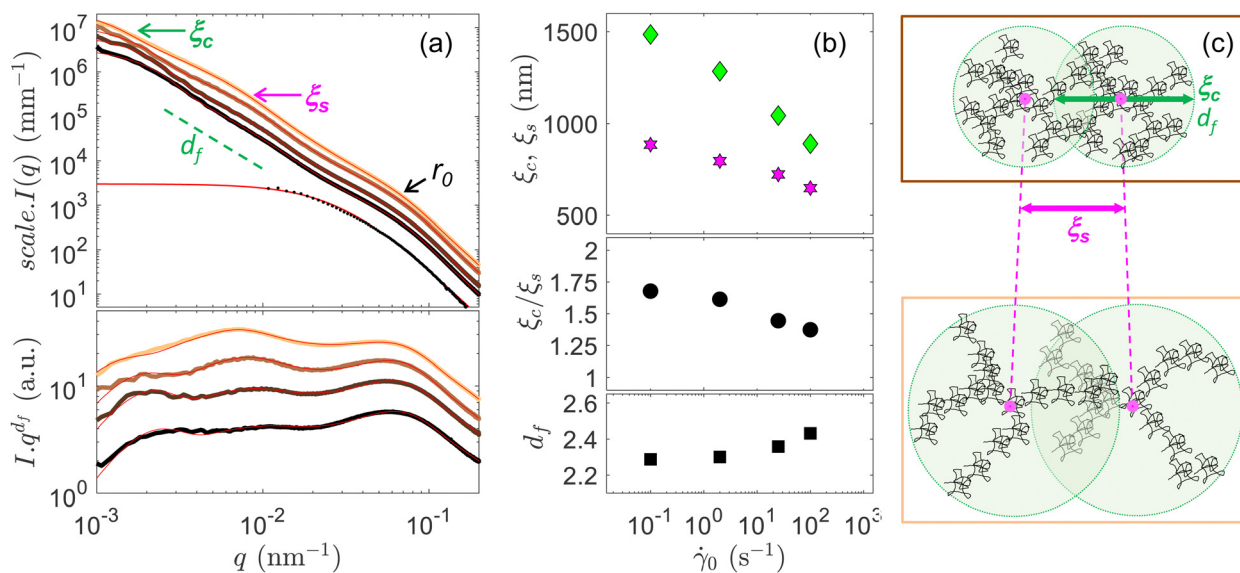

Fig. 6 Structure of the gel obtained after flow cessation. The scattering intensity $I(q)$ is measured 360 s after the end of the flow cessation test for different preshear $\dot{\gamma}_0$ in carbon black dispersions at $c_w = 4\%$. (a) The thick lines represent the evolution of $I(q)$ (top) and $I \cdot q^{d_f}$ (bottom) as a function of the wave vector q. Color codes from pink to black for $\dot{\gamma}_0 = 0.1$, 2, 20 and 100 s^{-1}. The dotted line is the form factor obtained at $c_w = 0.1\%$. Red lines are fit to the experimental data by a two-level Beaucage model composed of the CB particles of radius r_0 and clusters of size ξ_c with the fractal dimension d_f, modified by an intercluster structure factor that accounts for the center-to-center distance ξ_s between the clusters. The scattering intensity $I(q)$ and $I \cdot q^{d_f}$ are translated along the y-axis for better readability. (b) Evolution of the fit parameters ξ_c (green diamond), ξ_s (pink star), ξ_c/ξ_s (circle), and d_f (square) as a function of $\dot{\gamma}_0$. For the four fits, we obtained the radius of gyration $r_0 = 28.5$ nm. (c) Schematic of the evolution of the clusters as the preshear $\dot{\gamma}_0$ decreases between the top and bottom panels.

cessation. A gel prepared with a lower shear intensity shows a larger and looser microstructure since ξ_c increases and d_f decreases for decreasing $\dot{\gamma}_0$. Considering the evolution of only those two parameters suggests a decrease of the gel elasticity for decreasing values of $\dot{\gamma}_0$, in stark contrast with our observations. However, ξ_c and d_f are not the only parameters, and the correlation length ξ_s, which corresponds to the cluster to cluster center distance, plays an important role. In particular, ξ_s is smaller than the cluster size ξ_c, indicating that the clusters interpenetrate each other. Such cluster interpenetration has recently been suggested in carbon black gels to interpret step-down shear rate rheology experiments.[56] In our case, for lower shear rate intensity $\dot{\gamma}_0$ prior to flow cessation, the ratio ξ_c/ξ_s increases, *i.e.*, the clusters become more interpenetrated, accounting for the reinforcement of the gel elasticity. We therefore hypothesize that the gel elasticity is related to the cluster interpenetration, increasing the elasticity of the gel network as compared to the case where clusters would be packed in a random close-packing configuration [Fig. 6(c)].

3.4 A structure-based model to account for the gel elasticity

There are numerous models accounting for the elastic properties of fractal gels derived from microscopic considerations, namely the ϕ-power law models, especially in the context of diffusion-limited cluster aggregation (DLCA) and reaction-limited cluster aggregation (RLCA).[13,57–65] However, these models do not take into consideration the case where shear history interferes with the gelation pathway activated by thermal energy. Therefore, unsurprisingly, such models cannot capture our observations (see Fig. 13 in Appendix A.7). These models notably predict that the cluster size ξ_c is set by its fractal dimension d_f, the particle volume fraction ϕ and the particle size r_0 in stark contrast with our observations where the shear applied prior to flow cessation appears as an additional key parameter that acts on the gel structure. Moreover, in these models, the elastic properties of colloidal gels are either connected to the local bending cost of the particle network or to the cluster connectivity. However, to the best of our knowledge, none of these approaches accounts for an overlap, or equivalently for an interpenetration, of two neighboring clusters.

Here, we introduce the interpenetration ϕ-power law model. This model is an implementation of the ϕ-power law models proposed in ref. 13, 64 and 65. In practice, we assume that the gel is composed of particles of size r_0 that form clusters of size ξ_c and fractal dimension d_f separated by a center-to-center distance ξ_s. If $\xi_s > \xi_c$, the clusters are independent and the dispersion is a fluid. However, if $\xi_s < \xi_c$, clusters interpenetrate each other and form a gel. We have mostly replaced the factor from the ϕ-power law models that account for the elasticity of two adjacent clusters by an elongation elasticity due to the interpenetration. We assumed a decomposition of the microscopic stiffnesses in three contributions as springs in series, namely the intra-cluster, the intermicroscopic, and the interpenetration, respectively. We additionally assumed that the interpenetration stiffness is negligible at the microscopic scale, thus dominating the macroscopic rheological behaviour.

The gel elastic modulus G'_∞ at low frequencies is calculated in Appendix A.8 and yields the following expression:

$$G'_\infty = \underbrace{\frac{U}{r_0\delta^2}}_{G_{CB}} \underbrace{\frac{1}{2}\left(\frac{\xi_c}{r_0}\right)^{d_f}\left(1+\frac{\xi_s}{2\xi_c}\right)^{\frac{d_f}{3}}\left(1-\frac{\xi_s}{\xi_c}\right)^{\frac{2d_f}{3}}}_{g_{Interp}} \underbrace{\phi\left(\frac{\xi_s}{r_0}\right)^{2-d_f}}_{g_{Net}} \quad (1)$$

This expression displays an elasticity that follows the hierarchical structural properties of the gel. G_{CB} is the elasticity arising from colloid–colloid interactions where U and δ are, respectively, the depth and the range of the carbon black attraction. g_{Interp} corresponds to the scaling that accounts for the cluster–cluster interpenetration and g_{Net} is the scaling attributed to the network formed by the clusters at the macroscopic scale.

To test the relevance of the interpenetration ϕ-power law model, we report in Fig. 4(c) the best fit of G_c as a function of the $\dot{\gamma}_0$ using eqn (1) with the values of the structural parameters inferred from Fig. 6(b), the fact that $G'_\infty = 0.3G_c$ (see Appendix A.8), and the sole adjustable parameter $G_{CB} = 9$ Pa. The model correctly captures the decrease of the elasticity of the gel network as $\dot{\gamma}_0$ increases. However, taking $U = 10k_BT$ and $\delta = 0.2r_0$, we obtain $G_{CB} \sim 2000$ Pa, a value much larger than the fit value: the model fails to capture the absolute value of the gel elasticity.

The interpenetration ϕ-power law model thus shows that cluster interpenetration accounts for the scaling of the mechanical properties of the gels and allows to rationalize the counter-intuitive observation that lower shear rate intensities before flow cessation yield stronger gels. Such results raise open questions, which are listed below.

4 Discussion

We have used mechanical shear to explore various configurations of carbon black gels. Starting from a fluidized state under an applied shear rate $\dot{\gamma}_0$, we use an abrupt flow cessation to trigger a liquid-to-solid transition. Varying $\dot{\gamma}_0$ allows us to tune the gel viscoelastic properties, whose spectrum can be mapped on a single master curve asymptotically defined at low frequencies by the elasticity of the gel network G_∞ and at high frequencies by the viscosity η of the background solvent. Coupling rheometry and SAXS, we have shown that the gel microstructure is composed of fractal clusters that interpenetrate each other, and the degree of interpenetration appears to be a key parameter contributing to the gel elasticity. We have validated this hypothesis by developing an interpenetration ϕ-power law model that accounts for the decrease of elasticity as $\dot{\gamma}_0$ increases.

4.1 Is the scaling behavior of the viscoelastic spectrum a consequence of an underlying superposition principle?

In light of the scaling behavior of the viscoelastic spectrum, it is tempting to interpret the master curve obtained by varying $\dot{\gamma}_0$ as the result of some shear-frequency superposition principle. Superposition principles in soft matter mechanics rely on the idea that dynamical processes in soft materials can be accessed

equivalently using time or frequency and another well-chosen variable. For example, time-temperature superposition in polymer melts[66] relies on the acceleration of all activated processes at high temperatures, enabling probing of longer effective time scales at high temperatures. In other words, the average relaxation time of the material changes with temperature without affecting the shape of its viscoelastic spectrum.

This is not what we observe here, for the rescaling of the viscoelastic spectrum, a shift along the frequency axis and a shift along the viscoelastic moduli are required. Such behavior has, however, been observed in different systems and still attributed to a superposition principle such as in colloidal low-methoxyl pectin[67] in the context of gelling time/relaxation time superposition, in protein condensates[68] in the context of aging Maxwell fluids, in triblock copolymer solutions[69] in the context of time-composition superposition, and in soft colloidal glasses[70,71] in the context of time-concentration superposition. In the case of carbon black gels subject to various shear rate intensities before flow cessation, the viscoelastic spectrum scaling is attributed to deep structural changes, such as the cluster fractal dimension d_f (the gel does not have self-similar structures) rather than changes in the dynamics. Such results rule out a superposition principle. In other words, it is possible to form carbon black gels with the same value of the elastic plateau G_∞ using different gels structures through shear history and concentration as shown in Fig. 5(c).

4.2 Physical origin of the gel structure

The multiple metastable gels formed following various shear preparations belong to the category of fractal gels. This is probably why our results do not match the trends observed in ref. 19 which belong to gels formed through arrested phase separation. We find clusters of fractal dimension $d_f \in [2.3, 2.5]$ larger than the prediction from diffusion-limited cluster aggregation DLCA where $d_f \sim 1.8$[8] or reaction-limited cluster aggregation RLCA where $d_f \sim 2.1$[9] but smaller than the value obtained for sheared fractal aggregates where $d_f \sim 2.6$.[57]

In our system, the Brownian time $\tau_B = R^3 6\pi\eta/k_B T \in [0.07; 1600]$ s is set by the diffusion of particles of size R ranging from the CB dimension $r_0 = 35$ nm to the cluster size $\xi_c \sim 1$ µm. τ_B compares to the time necessary for flow cessation to take place $\tau_{fc} < 4$ s (Fig. 3) supporting again the fact that aggregation and flow cessation are coupled.

The interplay between flow and structure in gels has been tackled mainly in the flow regime[34,72] but has not been formalized to model multiple metastable gel states induced by a shear protocol. This is an important challenge in the pursue of memory materials[73] that aim to encode, access, and erase signatures of history in the state of a system.

The flow cessation protocol inducing the sol–gel transition could be addressed qualitatively through the use of the Mason number Mn,[74,75] which is here in the range $[3.5 \times 10^{-4}, 5.2]$ and agrees rather well with the values in ref. 75 and 76 or the adhesion number Ad,[77–79] which is here in the range $[3.6, 5.5 \times 10^4]$ weighing the relative importance of adhesion forces compared to shear forces and quantitatively using

coagulation–fragmentation equation[80–82] which embraces the competition between different aggregation mechanism and fragmentation through shear or collisions.

Finally, we suggest another way to apprehend the multiple metastable gels formed through flow cessation. Indeed, carbon black gels as many other systems display delayed yielding,[83–85] *i.e.*, when pushed at a constant shear stress σ, the gel initially at rest will start flowing on time scales that decrease exponentially with increasing value of σ. Our results prompt us to revisit delayed yielding phenomena and answer the following questions: how does gel prepared through flow cessation impact the delayed yielding mechanism? Is delayed yielding still characterized by an Arrhenius law? If so, is the energy barrier necessary to flow in the delayed yielding experiment related to the energy barrier to form the gel state induced by flow cessation?

5 Conclusions

In conclusion, we have quantified the impact of shear history on the viscoelastic properties of carbon black gels. We observe that, for a fixed content in nanoparticles, low shear intensities yield strong gels upon flow cessation, whereas larger shear intensities yield weaker gels. Such a variation in the gel strength was linked to the degree of interpenetration of the clusters that compose the gel microstructure. In that framework, we have introduced a mechanical model, the interpenetration ϕ-power law model, that captures the impact of shear history on the gel elasticity, yielding a prediction for the scaling exponent that links the gel elasticity to the gel structural properties. These results highlight the power of shear history as an experimental tool to tune the viscoelastic properties of colloidal gels without changing the content in nanoparticles or their interactions.

The viscoelastic spectrum[36] and the non-linear gel properties such as delayed yielding[84] observed in the carbon black gels are also observed in many other colloidal gels; we therefore believe that cluster interpenetration could also be quite a general concept applicable in attractive colloidal systems. In addition, our work raises several fundamental questions, such as predicting for any type of colloids, the respective contributions of cluster interpenetration, cluster connectivity, and bending to a colloidal gel elasticity. Finally, future work could focus on determining the role of cluster interpenetration in the gel non-linear mechanical response, which might be a versatile parameter to tune the failure scenario of soft viscoelastic gels.

Author contributions

T. G. supervised the project; T. G., S. M. and T. D. conceived and designed the experiments; N. D., L. M. and T. G. carried out the measurements; N. D., A. P. and T. G. analyzed the experiments. L. V. B. developed the rheology model. T. G. wrote the paper; T. D. edited the manuscript.

Conflicts of interest

There are no conflicts to declare.

A Appendix

A.1 Carbon black particles

Fig. 7 shows the scattering intensity *vs.* wave vector q for a dilute dispersion of CB particles (Vulcan PF, Cabot). Individual CB particles are fractal-like particles composed of fused nanoparticles of carbon,[29,32] which motivates the use of a mass fractal model[86] to fit $I(q)$. The fit yields a radius of gyration $r_g = 35$ nm with 20% polydispersity and a fractal dimension $d_{f0} = 2.9$. Density measurements of CB powder were performed using a helium pycnometer (AccuPyc II 1340, Micromeritics). Before the measurements, the powder was dried in an oven at 80 °C for 72 hours (2% in weight was lost). Two sets of measurements were done with 5 measurements in a row for the first sample ($m = 0.8619$ g) and 10 measurements in a row for the second sample ($m = 0.779$ g). The samples were poured into a 10 cm³ aluminum vessel. We obtained a density of the carbon black particles $d_{cb} = 2.26 \pm 0.03$.

A.2 Flow properties of carbon black gels

Fig. 8 reports the flow curve $\sigma(\dot{\gamma})$ of a $c_w = 4\%$ w CB dispersion obtained by a decreasing ramp of shear rate. The flow curve is fitted with a Herschel–Bulkley model, $\sigma = \sigma_y + K\dot{\gamma}^n$, and yields a dynamical yield stress $\sigma_y = 4.5$ Pa, a fluidity index $n = 0.83$, and a consistency index $K = 1.0$ Pa s$^{1/0.83}$. In Fig. 8, we also show the flow curve extracted from the preshear at $\dot{\gamma}_0$. We observe that those flow curves are not stationary. This is mostly due to the fact that the dispersion needs time to adapt from the jump in shear from 1000 s^{-1} to $\dot{\gamma}_0$.

A.3 Evolution of the viscoelastic modulus during the rest

During the rest period that follows the flow cessation protocol, we measured the viscoelastic moduli of the dispersion in its
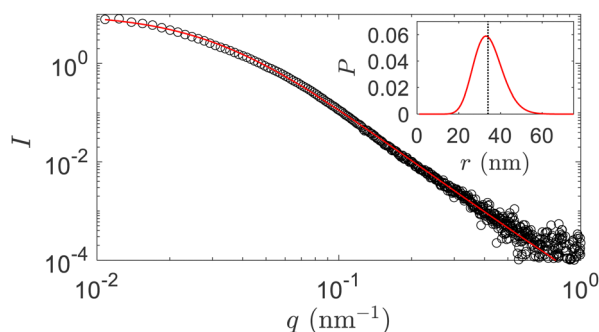

Fig. 8 Flow curve of the carbon black dispersion at $c_w = 4\%$ w showing the evolution of the measured stress σ as a function of the imposed shear rate $\dot{\gamma}$. $\dot{\gamma}$ is ramped down then up between 1500 s^{-1} and 0.015 s^{-1} with 10 points per decade at a rate of one point every 1 s. The red line is a Herschel–Bulkley fit. Unstationnary flow curve extracted from the pre-ashear at $\dot{\gamma}_0$ in Fig. 3b at $t = 1$ s ($\times$), at the maximum of σ (+) and at the end of the protocol (*).

Fig. 9 Evolution of the viscoelastic moduli during the rest just after the Flow cessation protocol. The viscoelastic moduli G' (line) and G'' (dash) are measured during 360 s at an oscillation amplitude of $\gamma = 0.1\%$ and a frequency of $f = 1$ Hz.

Fig. 7 Scattering intensity I *vs.* scattering wave number q of dilute dispersion of carbon black Vulcan PF nanoparticles in the RTM17 mineral oil ($c_w = 0.01\%$). The red line is a mass fractal fit of such a form factor using a fractal dimension $d_{f0} = 2.9$ and a Schulz particle radius distribution $P(r)$ centered on a radius of gyration $r_g = 35$ nm (dashed line) with a polydispersity of 20% as shown in the inset.
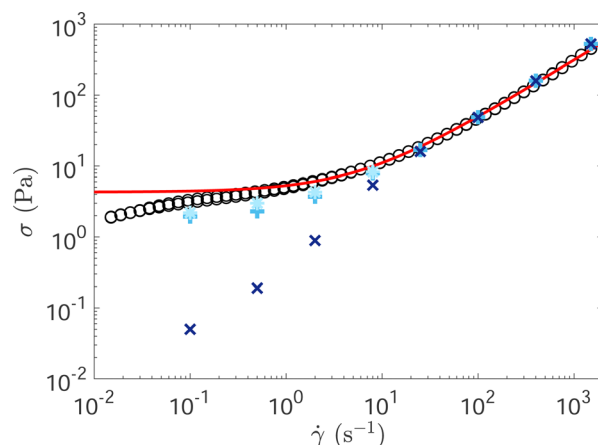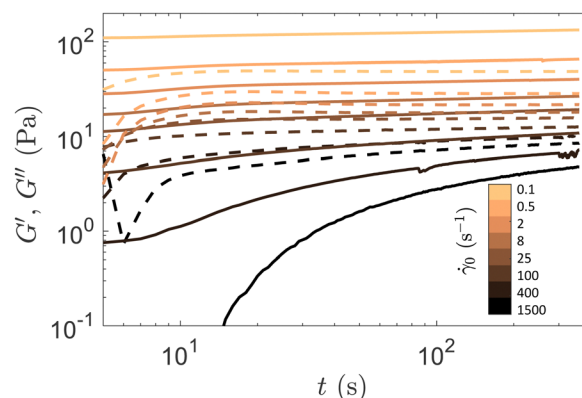
linear regime, Fig. 9. For high $\dot{\gamma}_0$, the gel reaches within $\sim$100 s a regime where aging becomes very slow. For low $\dot{\gamma}_0$, this slow aging regime is reached within a few seconds.

A.4 tan (δ) representation of the viscoelastic spectrum

Alternatively, the viscoelastic spectra plotted in Fig. 4a may be represented by $\tan(\delta) = G''/G'$ as a function of the frequency f, Fig. 10a. In this representation, $\tan(\delta) > 1$ indicates that dissipation dominates the rheological behavior whereas $\tan(\delta) < 1$ indicates a solid-like behavior at the corresponding frequency. In Fig. 4b, the viscoelastic spectrum is rescaled according to the coordinate (f_c, G_c). In the $\tan(\delta)$ representation as G' and G'' are rescaled by the same factor G_c only the frequency axis needs to be rescaled. The $\tan(\delta)$ measured for different $\dot{\gamma}_0$ scales on a master curve is displayed in Fig. 10b.
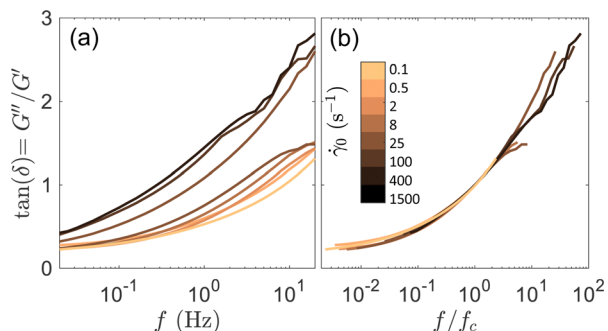
Fig. 10 The tan(δ) representation of the viscoelastic spectrum measured in Fig. 4a and b: (a) tan(δ) as a function of the frequency f and (b) tan(δ) as a function of the normalized frequency f/f_c.

A.5 Model for the normalized viscoelastic spectrum of carbon black gels

The master curve reported in Fig. 6 is fitted using a Kelvin–Voigt model and a fractional Kelvin–Voigt model,[87] as illustrated in Fig. 11. The fractional Kelvin–Voigt model consists of two springpots in parallel, defined by their quasi-properties ($\mathbb{V}$, $\mathbb{E}$) and their dimensionless exponents (α, β). Each springpot can be understood as a mechanical element having intermediate properties between that of spring when its exponent is 0 and a dashpot when its exponent is 1. The resolution of the fractional Kelvin–Voigt model leads to

$$\begin{cases} G' = \mathbb{E}f^{\beta}\cos(\beta\pi/2) + \mathbb{V}f^{\alpha}\cos(\alpha\pi/2) \\ G'' = \mathbb{E}f^{\beta}\sin(\beta\pi/2) + \mathbb{V}f^{\alpha}\sin(\alpha\pi/2) \end{cases} \quad (2)$$

In the limit where $\alpha = 1$ and $\beta = 0$, we recover the classical Kelvin–Voigt model, which is defined by a dashpot of viscosity η in parallel with a spring of elasticity G_{∞}.

$$\begin{cases} G' = \mathbb{E} = G_{\infty} \\ G'' = \mathbb{V}f = 2\pi\eta f \end{cases} \quad (3)$$

As shown in Fig. 11, the fractional model fits relatively well the normalized viscoelastic spectrum of carbon black gels in mineral oil using ($\mathbb{V}/G_c = 0.56$, $\alpha = 0.91$) and ($\mathbb{E}/G_c = 1.09$, $\beta = 0.11$). Its classical counterpart can only capture the asymptotic behavior of the viscoelastic spectrum, $i.e.$, the network elasticity $G_{\infty} = G'(f \ll f_c)$ and the background viscosity $\eta = G''(f \gg f_c)/(2\pi f)$. We note that $G_{\infty} = 0.3G_c$.

A.6 Influence of the concentration c_w

Following the protocol displayed in Fig. 2, we test the influence of the concentration for $c_w = 2$, 3, 6 and 8% in addition to $c_w = 4$%. Such concentration series are presented in Fig. 12 for $\dot{\gamma}_0 = 1500$ s^{-1}. We observe that high concentrations shift the viscoelastic spectrum to higher elasticities. The cross over point is not always reachable within the frequency window. We scale the viscoelastic spectrum G', G'' on the master curve displayed in Fig. 4b to determine (f_c, G_c) and plot the results in Fig. 5.

Fig. 12 Evolution of the viscoelastic spectrum for different gel concentration c_w at $\dot{\gamma}_0 = 1500$ s^{-1}. (a) G' (line) and G'' (dash) as a function of f. The concentration varied from $c_w = 2$ (blue) to 8% (green). (b) Rescaled viscoelastic spectrum. The grey curves are taken from ref. 41 and correspond to the master curve obtained by scaling a concentration series of carbon black dispersion in oil.
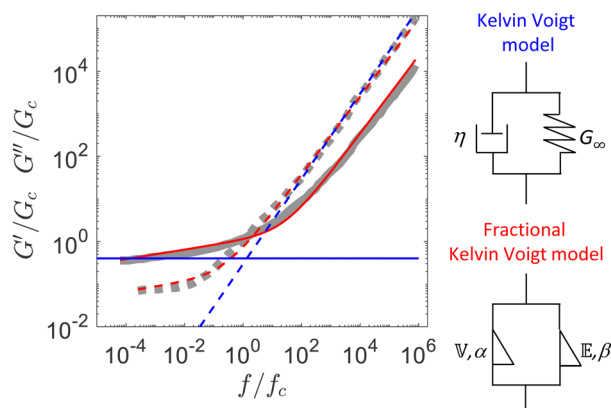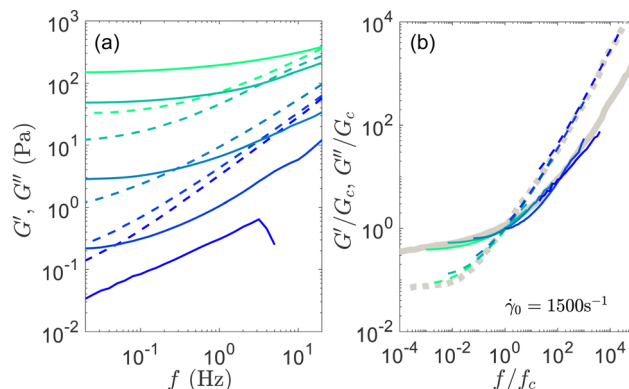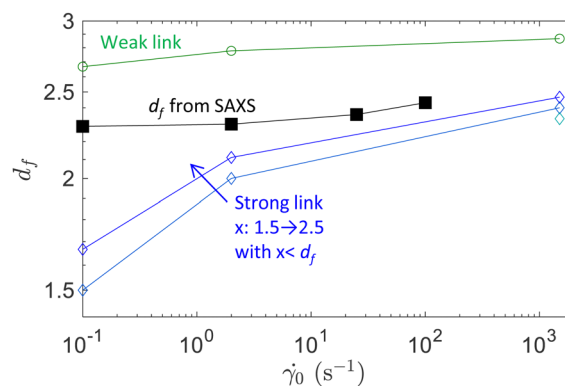

Fig. 11 Model of the normalized viscoelastic spectrum. Evolution of the normalized elastic G'/G_c (grey line) and viscous G''/G_c (dashed grey line) moduli as a function of the frequency f/f_c, extracted from ref. 41 (f_c, G_c) are the coordinates of the crossover between G' and G''. The Kelvin–Voigt model is pictured in blue and the fractional Kelvin–Voigt model in red.

Fig. 13 Fractal dimension d_f as a function of the shear step $\dot{\gamma}_0$. Measurements of d_f extracted from the SAXS fit in Fig. 6 (square) and evaluated from Fig. 5 using the weak link model (circle) and the strong link model (diamond) from ref. 13. The fractal dimension x of the gel backbone has been varied from $x = 1.5$ (light blue) to $x = 2.5$ (dark blue) in the strong link model.

Soft Matter

A.7 Analysis of the rheo-SAXS data

The CB gel scattered intensities $I_{rad}(q)$ and $I_{tan}(q)$ are, respectively, measured in the radial and the tangential configuration. In the radial configuration, the X-ray beam probes the microstructure in the flow-vorticity plane, while in the tangential configuration, the X-ray beam probes the sample along the velocity gradient-vorticity plane as a sketch in Fig. 14. After the rest of the protocol from Fig. 2, the radial and tangential scattered intensities are compared. More precisely the radial scattering I_{rad} is decomposed in its perpendicular $I_{rad\perp}$ and parallel $I_{rad\parallel}$ components. In Fig. 14, we observe that $I_{tan} = I_{rad\perp} = I_{rad\parallel}$. The scattering intensity is isotropic and equal in all configurations. For better statistics, we focus on the tangential signal and radially average its 2D spectrum. In the paper, we note $I(q) = I_{tan}(q)$.

The intensity scattered by the carbon black is fitted in a log scale using a modified Beaucage model,[54,55,88] Fig. 15:

$$
\begin{aligned}
I(q) &= \underbrace{\left[G_1 \exp\left(-\frac{q^2 r_1^2}{3}\right)^2 + B_1 \exp\left(-\frac{q^2 r_2^2}{3}\right) q_1^{*p_1} \right]}_{\text{Beaucage, Cluster level, } I_1} \\
&\times \underbrace{\left[1 + C_0 \left(\left(\frac{q}{q_s}\right)^2 + \left(\frac{q_s}{q}\right)^2 \right)^{-1} \right]}_{\text{Inter-Cluster structure, } S_1} \\
&+ \underbrace{\left[G_2 \exp\left(\left(-\frac{q^2 r_2^2}{3}\right)^2 + B_2 q_2^{*p_2} \right)^{-1} \right]}_{\text{Inter-Cluster structure, } I_1}
\end{aligned}
\tag{4}
$$

$$
\text{with} \quad q_{i=1,2}^* = q\left(\text{erf}\left(\frac{q r_i}{\sqrt{6}}\right) \right)^{-3}
$$

In eqn (4), $I_2(q)$ refers to scattering due to the CB particle of size $r_0 = r_2$ and fractal dimension $d_{f0} = -p_2$. The scattering due to the clusters of size $\xi_c = r_1$ and fractal dimension $d_f = -p_1$ is contained in the term $I_1(q)$. The modification of the two-level Beaucage model consists in introducing an inter-cluster structure factor $S_1(q)$ that accounts for the center-to-center distance
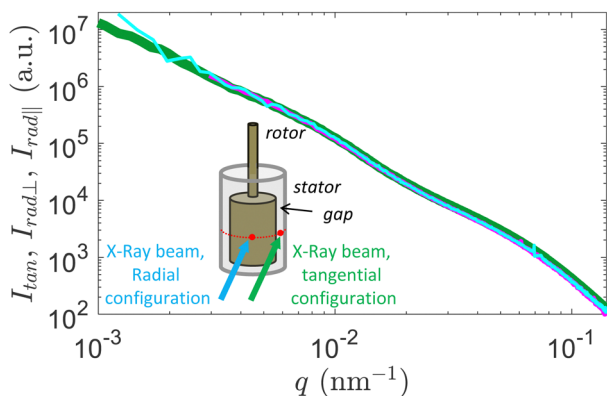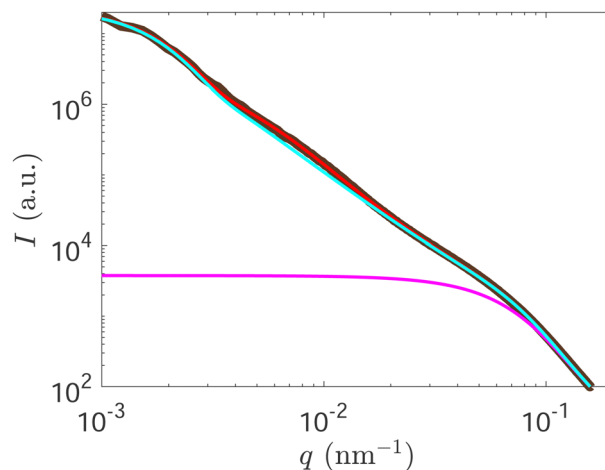

Fig. 15 Decomposition of the modified Beaucage model as written in eqn (4). Scattering intensity $I(q)$ as a function of q: experimental data (black), I_2 (pink), $I_1 + I_2$ (cyan), $I_1 \cdot S_1 + I_2$ (red).

between adjacent clusters, $\xi_s = 2\pi/q_s$. $S_1(q)$ is a function that peaks at q_s to a maximum value $S_1(q_s) = 1 + C_0/2$ and that converges to 1 away from q_s.

This fit is constrained by mass conservation. Indeed, as the multi-stable gels result from the same carbon black dispersion, all the gels have the same average number of particles at the macroscopic scale and in their unit cell. The unit cell is the minimum structural repeating unit necessary to construct the gel. In our case, the gel network unit cell is defined by the structural length ξ_s. The number of particles $N = (\xi_c/r_0)^{d_f}$ in a unit cell corresponds to the number of particles in the cluster of size ξ_c and fractal dimension d_f. This gives a particle density $\rho = \dfrac{(\xi_c/r_0)^{d_f}}{\xi_s^3} = \text{cste}$. This constraint is well verified based on parameters obtained by fitting the SAXS data. As shown in Fig. 16, $\rho = 7250 \pm 230$ particles per μm^3 is constant within a margin of error of 3%. Moreover, ρ can be related to the particle concentration c_w provided a good knowledge of the background oil density $d_{bck} = 0.871$ ($T = 20\ ^\circ C$), the individual carbon black particle density $d_{cb} = 2.26 \pm 0.03$ ($T = 20\ ^\circ C$) and the volume of a carbon black particle v_{cb}. The carbon black density ρ in the gel

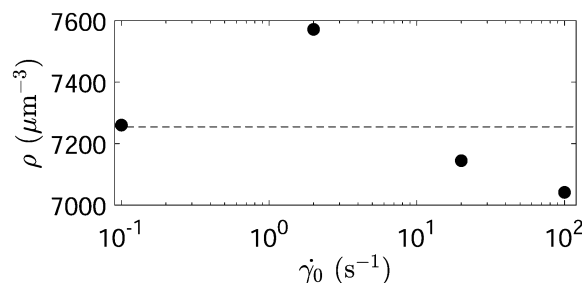Fig. 14 Comparison of the scattering intensity between the tangential I_{tan} (green) and radial $I_{rad\perp}$ (cyan) $I_{rad\parallel}$ (magenta) configuration.

Fig. 16 Density of particles per unit cell ρ as the function of the step shear $\dot{\gamma}_0$. ρ is calculated from the values r_0, ξ_c, d_f and ξ_s obtained fitting the scattering intensity $I(q)$ plotted in Fig. 6a with eqn (4). The dashed line is the average.

is then

$$\rho = \frac{\phi}{v_{cb}}, \quad \text{with } \phi = \frac{c_w}{\left(c_w + \frac{d_{cb}}{d_{bck}}(1 - c_w)\right)} \quad (5)$$

As it is hard to measure ν_{cb} given the particle fractal nature, ν_{cb} was evaluated from ρ. Using $v_{cb} = 4/3\pi r_\rho^3$ we obtain $r_\rho = 8.1$ nm a value lower than the radius of gyration of 35 nm extracted from the form factor measured in SAXS Fig. 7. This value is a bit smaller because the CB particles are fractal and polydisperse. Moreover, SAXS measurements tend to over-estimate the particle size distribution as SAXS is more sensitive to larger particles. Finally, we might overestimate ρ as we assumed that the clusters pack the space homogeneously. Despite the fact that r_ρ is slightly small, we find $\rho = $ cste which tells us that the model is self-consistent.

A.8 The interpenetration ϕ-power law model, a model of the gel elasticity based on scaling arguments

We assume that the gel is composed of particles of size r_0 that form clusters of size ξ_c and fractal dimension d_f separated by a center-to-center distance ξ_s. If $\xi_s > \xi_c$, the clusters are inde-pendent and the dispersion is a fluid. However, if $\xi_s < \xi_c$, clusters interpenetrate each other and form a gel. To model the elastic constant of the gel network, we follow the demonstra-tions of the ϕ-power law models proposed in ref. 13, 64 and 65 which allows us to write

$$G'_\infty = \frac{K}{L} \quad (6)$$

$$K = \left(\frac{L}{\xi_s}\right)^{\dim - 2} K_{eff} \quad (7)$$

$$\phi\left(\frac{\xi_s}{r_0}\right)^{3 - d_f} = \left(\frac{\xi_s}{L}\right)^{3 - \dim} \quad (8)$$

with G'_∞ being the linear storage modulus, ϕ the particle volume fraction, K the macroscopic stiffness of the gel, L the macroscopic size, K_{eff} the elementary effective stiffness of clusters and dim the dimension of the network which can be equal to the dimension of the euclidean space. These ϕ-power law models are based on building the relationship between a microscopic stiffness due to the interaction potential between the colloids and a macroscopic scale through different extra-polation by means of scaling laws. Then, to demonstrate our interpenetration ϕ-power law model, we assume that K_{eff} may be written as follows:

$$\frac{1}{K_{eff}} = \frac{1}{K_c} + \frac{1}{K_{ext}} + \frac{1}{K_i} \quad (9)$$

with K_c, K_{ext} and K_i being the elastic stiffness related to the inside of the cluster, the intermicroscopic (see ref. 65) and the interpenetration of the cluster, respectively. These different stiffnesses are considered as spring in series as a sketch in Fig. 17 and as commonly assumed in the literature.[65]
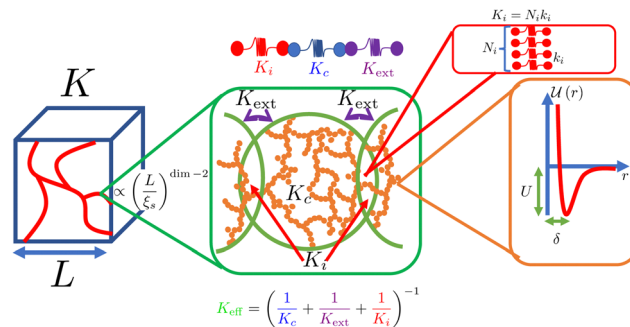

Fig. 17 Sketch of the contributions to the gel elasticity associated with the hierarchical structure of the gel.

Let us now quantify K_i. K_i is assumed to be proportional to the number of contact N_i between interpenetrating clusters: $K_i = N_i k_i$, where k_i is a reference interpenetration stiffness. The last expression comes from the fact we assumed that the contacts in the interpenetration zone are parallel springs: this justifies the additivity of the stiffnesses. This point has never been highlighted in the literature and is part of our proposition for the interpenetration ϕ-power law model. Also, the reference interpenetration stiffness k_i is a hard point in the model. Indeed, referring to ref. 58 and 59, there may be a competition between elongation stiffness and bending stiffness. Without any true experimental insights about the interpenetration zone, it is hard to disentangle the contribution of each and we will assume that it is directly related to the depth of the interaction potential U and the distance of interaction δ through $k_i = U/\delta^2$.

Due to the fractal nature of the clusters, there are $N_i = \left(6V_i/\pi r_0^3\right)^{\frac{d_f}{3}}$ particles inside the intersection volume V_i between two clusters. Geometrically assimilating clusters to spheres lead to an intersection volume (ref. 89 and 90, p. 97)

$$V_i = \frac{\pi}{12}\xi_c^3\left(2 + \frac{\xi_s}{\xi_c}\right)\left(1 - \frac{\xi_s}{\xi_c}\right)^2 1_{\{\xi_s < \xi_c\}}. \quad (10)$$

we assume that each particle brought by each cluster in V_i forms a contact adding rigidity to the whole system. Therefore, the number of contact is roughly N_i. Putting together the last expressions, we get

$$K_i = \frac{U}{2\delta^2}\left(\frac{\xi_c}{r_0}\right)^{d_f}\left(1 + \frac{\xi_s}{2\xi_c}\right)^{\frac{d_f}{3}}\left(1 - \frac{\xi_s}{\xi_c}\right)^{\frac{2d_f}{3}} 1_{\{\xi_s < \xi_c\}}. \quad (11)$$

Let us now compare K_i with K_c and K_{ext}. There are different ways to consider that $K_i \ll \min(K_c, K_{ext})$. To simplify the compari-son, following ref.65, we will write

$$\frac{1}{K_c} + \frac{1}{K_{ext}} = \frac{1}{K_c}\left(\frac{K_c}{K_{ext}}\right)^\alpha \quad (12)$$

with $\alpha \in [0,1]$ allowing to make a transition between the weak-link regime and the strong-link regime. A first way to compare K_i with $K_c(K_{ext}/K_c)^\alpha$ is to say that the system is in the regime
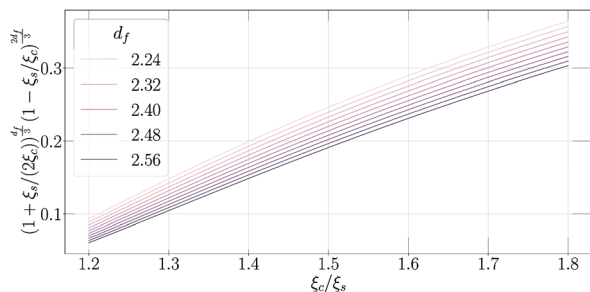
Fig. 18 Evolution of $\xi_c/\xi_s \mapsto (1 + \xi_s/(2\xi_c))^{\frac{d_f}{3}}(1 - \xi_s/\xi_c)^{\frac{2d_f}{3}}$ for different values of d_f on [1.2,1.8].

$\xi_c/\xi_s \gtrsim 1$. Thus, one can re-write eqn (11) as

$$K_i \underset{\xi_c/\xi_s \gtrsim 1}{\propto} \frac{U}{2\delta^2}\left(1 - \frac{\xi_s}{\xi_c}\right)^{\frac{2d_f}{3}} \qquad (13)$$

telling us that K_i depends strongly on the distance of ξ_c/ξ_s from unity. Therefore, K_i is negligible when $\xi_c/\xi_s \gtrsim 1$ compared to $K_c(K_{ext}/K_c)^\alpha$ and eqn (9), we get $K_{eff} \approx K_i$.

The other way to consider the system is, following previous approaches in ref. 13, 57–59, 64 and 65 estimating $K_c(K_{ext}/K_c)^\alpha \propto \xi_s^{-\mu}$ with $\mu \in [1,5]$ function of the fractal dimension d_f, the dimension of the elastic backbone and the regime of strong-link or weak-link because ξ_s is similar to a cluster size with contact. Recalling that $(\xi_c/r_0)^{d_f} \propto \xi_s^3$, one gets in this case

$$\frac{K_i}{K_c}\left(\frac{K_c}{K_{ext}}\right)^\alpha \propto \xi_s^{3+\mu}\left(1 + \frac{\xi_s}{2\xi_c}\right)^{\frac{d_f}{3}}\left(1 - \frac{\xi_s}{\xi_c}\right)^{\frac{2d_f}{3}}. \qquad (14)$$

Assuming that ξ_s does not vary much, $K_i/K_c(K_c/K_{ext})^\alpha$ is governed by the values of $\xi_c/\xi_s \mapsto (1 + \xi_s/(2\xi_c))^{\frac{d_f}{3}}(1 - \xi_s/\xi_c)^{\frac{2d_f}{3}}$ on [1.2,1.8]. Referring to Fig. 18, $K_i/K_c(K_c/K_{ext})^\alpha$ is between 0.1 and 0.3. Therefore, one can assume that $K_i \ll K_c(K_{ext}/K_c)^\alpha$, at least for the first values, and following eqn (9), we get $K \approx K_i$.

Generally, the more K_i is getting closer to $K_c(K_{ext}/K_c)^\alpha$, the more difficult it is to consider that only one phenomenon prevails. If someone wants to completely understand the balance between the different contributions, she or he needs to model both phenomena and their coupling. This is not the goal of this model which tries to give some orders of magnitude without exhaustively modeling the system.

This final expression of the interpenetration ϕ-power law model is then

$$G'_\infty = \underbrace{\frac{U}{r_0\delta^2}}_{G_{CB}} \frac{1}{2}\underbrace{\left(\frac{\xi_c}{r_0}\right)^{d_f}\left(1 + \frac{\xi_s}{2\xi_c}\right)^{\frac{d_f}{3}}\left(1 - \frac{\xi_s}{\xi_c}\right)^{\frac{2d_f}{3}}}_{g_{Interp}}\underbrace{\phi\left(\frac{\xi_s}{r_0}\right)^{2-d_f}}_{g_{Net}} \qquad (15)$$

explicating that G_{CB} corresponds to the elasticity arising from colloid–colloid interaction with U and δ, respectively, the depth and the range of the attraction, g_{Interp} is the elementary scaling for elasticity to account for interpenetration and may be changed according to ref. 13 and g_{Net} is the network contribution from the element of elasticity to the macroscopic scale. The dimension of the network dim is not required in the final

expression due to the contribution of the effective volume fraction through the particle volume fraction and the fractal dimension related to ξ_s.

The difference with the usual ϕ-power law model[13] relies on the fact that $K_i = N_ik_i$ for our interpenetration ϕ-power law model and $K_i = (\xi_s/r_0)^{-2-x}k_i$ with x the chemical dimension or the dimension of the elastic backbone for the usual ϕ-power law model.[13] If we assume dim = 3, it is possible to find a weak-link-like regime[13] with $G'_\infty \propto \phi^{\frac{1}{3-d_f}}$.

To summarize the approach and the assumptions:

• Most of the ingredients come from the previous ϕ-power law models building elasticity from microscopic quantities.[13,64,65] The scaling between the macroscopic stiffness and the effective microscopic stiffness is conserved, the colloid–colloid interaction is conserved without expliciting the relations with bending or elongation, and the construction of the effective microscopic stiffness as spring in series is also conserved.

• We assumed the domination in the behaviour of K_i instead of the other stiffnesses, at least at the beginning of the interpenetration. As discussed above, the more pronounced the interpenetration, the more questionable this hypothesis. In a fully interpenetrated case, the contribution of each phenomenon may be of the same order of magnitude and the previous demonstration does not hold anymore. The derivation of an exhaustive model allowing the transition from one case to the other will be out of the scope of this paper. However, we encourage future research to dig into this model to make it complete and exhaustive against the literature and the present results.

Acknowledgements

Notes and references

1 V. Trappe, V. Prasad, L. Cipelletti, P. Segre and D. A. Weitz, *Nature*, 2001, **411**, 772–775.

2 P. Lu and D. Weitz, *Annu. Rev. Condens. Matter Phys.*, 2013, **4**, 217–233.

3 K. Ioannidou, M. Kanduc, L. Li, D. Frenkel, J. Dobnikar and E. D. Gado, *Nat. Commun.*, 2016, **7**, 12106.

4 H. Parant, G. Muller, T. Le Mercier, J. Tarascon, P. Poulin and A. Colin, *Carbon*, 2017, **119**, 10–20.

5 Y. Cao and R. Mezzenga, *Nat. Food*, 2020, **1**, 106–118.

6 V. Trappe and P. Sandkühler, *Curr. Opin. Colloid Interface Sci.*, 2004, **8**, 494–500.

7 E. Zaccarelli, *J. Phys.: Condens. Matter*, 2007, **19**, 323101.

8 D. Weitz and M. Oliveria, *Phys. Rev. Lett.*, 1984, **52**, 1433.

9 D. W. Schaefer, J. E. Martin, P. Wiltzius and D. S. Cannell, *Phys. Rev. Lett.*, 1984, **52**, 2371.

10 F. Cardinaux, T. Gibaud, A. Stradner and P. Schurtenberger, *Phys. Rev. Lett.*, 2007, **99**, 118301.

11 P. J. Lu, E. Zaccarelli, F. Ciulla, A. B. Schofield, F. Sciortino and D. A. Weitz, *Nature*, 2008, **453**, 499–503.

12 R. N. Zia, B. J. Landrum and W. B. Russel, *J. Rheol.*, 2014, **58**, 1121–1157.

13 W.-H. Shih, W. Y. Shih, S.-I. Kim, J. Liu and I. A. Aksay, *Phys. Rev. A: At., Mol., Opt. Phys.*, 1990, **42**, 4772.

14 A. H. Krall and D. A. Weitz, *Phys. Rev. Lett.*, 1998, **80**, 778–781.

15 A. Zaccone, H. Wu and E. Del Gado, *Phys. Rev. Lett.*, 2009, **103**, 208301.

16 K. A. Whitaker, Z. Varga, L. C. Hsiao, M. J. Solomon, J. W. Swan and E. M. Furst, *Nat. Commun.*, 2019, **10**, 1–8.

17 T. Gibaud, A. Zaccone, E. Del Gado, V. Trappe and P. Schurtenberger, *Phys. Rev. Lett.*, 2013, **110**, 058303.

18 T. Gibaud and P. Schurtenberger, *J. Phys.: Condens. Matter*, 2009, **21**, 322201.

19 N. Koumakis, E. Moghimi, R. Besseling, W. C. Poon, J. F. Brady and G. Petekidis, *Soft Matter*, 2015, **11**, 4640–4648.

20 A. Helal, T. Divoux and G. H. McKinley, *Phys. Rev. Appl.*, 2016, **6**, 064004.

21 M. Utz, P. G. Debenedetti and F. H. Stillinger, *Phys. Rev. Lett.*, 2000, **84**, 1471–1474.

22 D. Bonn, H. Tanaka, P. Coussot and J. Meunier, *J. Phys.: Condens. Matter*, 2004, **16**, S4987.

23 E. Moghimi, A. R. Jacob, N. Koumakis and G. Petekidis, *Soft Matter*, 2017, **13**, 2371–2383.

24 G. Ovarlez, L. Tocquer, F. Bertrand and P. Coussot, *Soft Matter*, 2013, **9**, 5540–5549.

25 J. R. Raney, B. G. Compton, J. Mueller, T. J. Ober, K. Shea and J. A. Lewis, *Proc. Natl. Acad. Sci. U. S. A.*, 2018, **115**, 1198–1203.

26 N. Dagès, P. Lidon, G. Jung, F. Pignon, S. Manneville and T. Gibaud, *J. Rheol.*, 2021, **65**, 477–490.

27 J. Lahaye and F. Ehrburger-Dolle, *Carbon*, 1994, **32**, 1319–1324.

28 J. Xi and B.-J. Zhong, *Chem. Eng. Technol.*, 2006, **29**, 665–673.

29 M. Sztucki, T. Narayanan and G. Beaucage, *J. Appl. Phys.*, 2007, **101**, 114304.

30 M.-J. Wang, *Carbon Black: Science and Technology*, Routledge, 2018.

31 C. R. Herd, G. C. McDonald and W. M. Hess, *Rubber Chem. Technol.*, 1992, **65**, 107–129.

32 R. F. Martinez, M. Iturrondobeitia, J. Ibarretxe and T. Guraya, *J. Mater. Sci.*, 2017, **52**, 569–580.

33 J. J. Richards, J. B. Hipp, J. K. Riley, N. J. Wagner and P. D. Butler, *Langmuir*, 2017, **33**, 12260–12266.

34 J. B. Hipp, J. J. Richards and N. J. Wagner, *J. Rheol.*, 2021, **65**, 145–157.

35 V. Trappe, E. Pitard, L. Ramos, A. Robert, H. Bissig and L. Cipelletti, *Phys. Rev. E: Stat., Nonlinear, Soft Matter Phys.*, 2007, **76**, 051404.

36 V. Prasad, V. Trappe, A. Dinsmore, P. Segre, L. Cipelletti and D. Weitz, *Faraday Discuss.*, 2003, **123**, 1–12.

37 W. Herschel and R. Bulkley, *Am. Soc. Test. Mater., Proc.*, 1926, 621–633.

38 M. Fardin, C. Perge and N. Taberlet, *Soft Matter*, 2014, **10**, 3523–3535.

39 T. Narayanan, M. Sztucki, T. Zinn, J. Kieffer, A. Homs-Puron, J. Gorini, P. Van Vaerenbergh and P. Boesecke, *J. Appl. Crystallogr.*, 2022, **55**, 98–111.

40 P. Panine, M. Gradzielski and T. Narayanan, *Rev. Sci. Instrum.*, 2003, **74**, 2451–2455.

41 V. Trappe and D. Weitz, *Phys. Rev. Lett.*, 2000, **85**, 449.

42 K. Dullaert and J. Mewis, *J. Rheol.*, 2005, **49**, 1213–1230.

43 S. P. Meeker, R. T. Bonnecaze and M. Cloitre, *J. Rheol.*, 2004, **48**, 1295–1320.

44 U. Zölzer and H.-F. Eicke, *Rheol. Acta*, 1993, **32**, 104–107.

45 C. Baravian and D. Quemada, *Rheol. Acta*, 1998, **37**, 223–233.

46 R. H. Ewoldt and G. H. McKinley, *Rheol. Bull.*, 2007, **76**, 4–24.

47 G. Benmouffok-Benbelkacem, F. Caton, C. Baravian and S. Skali-Lami, *Rheol. Acta*, 2010, **49**, 305–314.

48 R. Radhakrishnan, T. Divoux, S. Manneville and S. M. Fielding, *Soft Matter*, 2017, **13**, 1834–1852.

49 Y.-Y. Won, S. P. Meeker, V. Trappe, D. A. Weitz, N. Z. Diggs and J. I. Emert, *Langmuir*, 2005, **21**, 924–932.

50 I. Sudreau, S. Manneville, M. Servel and T. Divoux, *J. Rheol.*, 2022, **66**, 91–104.

51 M. Das and G. Petekidis, 2022, arXiv:2207.05185.

52 R. Buscall, P. D. Mills, J. W. Goodwin and D. Lawson, *J. Chem. Soc., Faraday Trans. 1*, 1988, **84**, 4249–4260.

53 E. Courtens and R. Vacher, *Z. Phys. B: Condens. Matter*, 1987, **68**, 355–361.

54 G. Beaucage, *J. Appl. Crystallogr.*, 1995, **28**, 717–728.

55 G. Beaucage, *J. Appl. Crystallogr.*, 1996, **29**, 134–146.

56 Y. Wang and R. H. Ewoldt, 2022, arXiv preprint arXiv:2202.05772.

57 R. Wessel and R. Ball, *Phys. Rev. A: At., Mol., Opt. Phys.*, 1992, **46**, R3008.

58 Y. Kantor and T. A. Witten, *J. Phys., Lett.*, 1984, **45**, 675–679.

59 Y. Kantor and I. Webman, *Phys. Rev. Lett.*, 1984, **52**, 1891–1894.

60 J. Mewis and N. J. Wagner, *Colloidal Suspension Rheology*, Cambridge Univesity Press, 2012.

61 A. G. Marangoni, *Phys. Rev. B: Condens. Matter Mater. Phys.*, 2000, **62**, 13951–13955.

62 A. J. Gravelle and A. G. Marangoni, *J. Colloid Interface Sci.*, 2021, **598**, 56–68.

63 V. I. Roldughin, *Russ. Chem. Rev.*, 2003, **72**, 913–937.

64 M. Mellema, J. H. J. van Opheusde and T. van Vliet, *J. Rheol.*, 2002, **46**, 11–29.

65 H. Wu and M. Morbidelli, *Langmuir*, 2001, **17**, 1030–1036.

66 M. Van Gurp and J. Palmen, *Rheol. Bull.*, 1998, **67**, 5–8.

67 S.-T. Huang, C.-H. Yang, P.-J. Lin, C.-Y. Su and C.-C. Hua, *Phys. Chem. Chem. Phys.*, 2021, **23**, 19269–19279.

68 L. Jawerth, E. Fischer-Friedrich, S. Saha, J. Wang, T. Franzmann, X. Zhang, J. Sachweh, M. Ruer, M. Ijavi and S. Saha, *et al.*, *Science*, 2020, **370**, 1317–1323.

69 A. S. Krishnan, S. Seifert, B. Lee, S. A. Khan and R. J. Spontak, *Soft Matter*, 2010, **6**, 4331–4334.

70 Y. H. Wen, J. L. Schaefer and L. A. Archer, *ACS Macro Lett.*, 2015, **4**, 119–123.

71 Y. H. Wen, Y. Lu, K. M. Dobosz and L. A. Archer, *Macromolecules*, 2014, **47**, 4479–4492.

72 M. Nabizadeh and S. Jamali, *Nat. Commun.*, 2021, **12**, 1–9.

73 N. C. Keim, J. D. Paulsen, Z. Zeravcic, S. Sastry and S. R. Nagel, *Rev. Mod. Phys.*, 2019, **91**, 035002.

74 Z. Varga and J. W. Swan, *J. Rheol.*, 2018, **62**, 405–418.

75 S. Jamali, R. C. Armstrong and G. H. McKinley, *Mater. Today Adv.*, 2020, **5**, 100026.

76 S. Jamali, R. C. Armstrong and G. H. McKinley, *Phys. Rev. Lett.*, 2019, **123**, 248003.

77 M. L. Eggersdorfer, D. Kadau, H. J. Herrmann and S. E. Pratsinis, *J. Colloid Interface Sci.*, 2010, **342**, 261–268.

78 J. S. Marshall and S. Li, *Adhesive Particle Flow: A Discrete-Element Approach*, Cambridge University Press, 32 Avenue of the Americas, NY 10013-2473, USA, 1st edn, 2014.

79 A. Kimbonguila Manounou and S. Rémond, *Physica A*, 2014, **412**, 66–83.

80 J. Banasiak, W. Lamb and P. Laurençot, *Analytic Methods for Coagulation-Fragmentation Models, Volume I*, CRC PressTaylor & Francis Group 6000, Broken Sound Parkway NW, Suite 300 Boca Raton, FL 33487-2742, 2020, vol. 1.

81 V. Stadnichuk, A. Bodrova and N. Brilliantov, *Int. J. Mod. Phys. B*, 2015, **29**, 1–10.

82 C. M. Sorensen, H. X. Zhang and T. W. Taylor, *Phys. Rev. Lett.*, 1987, **59**, 363–366.

83 T. Gibaud, D. Frelat and S. Manneville, *Soft Matter*, 2010, **6**, 3482–3488.

84 J. Sprakel, S. B. Lindström, T. E. Kodger and D. A. Weitz, *Phys. Rev. Lett.*, 2011, **106**, 248303.

85 V. Grenard, T. Divoux, N. Taberlet and S. Manneville, *Soft Matter*, 2014, **10**, 1555–1571.

86 J. Teixeira, *J. Appl. Crystallogr.*, 1988, **21**, 781–785.

87 H. Schiessel, R. Metzler, A. Blumen and T. Nonnenmacher, *J. Phys. A: Math. Gen.*, 1995, **28**, 6567.

88 B. Keshavarz, D. G. Rodrigues, J.-B. Champenois, M. G. Frith, J. Ilavsky, M. Geri, T. Divoux, G. H. McKinley and A. Poulesquen, *Proc. Natl. Acad. Sci. U. S. A.*, 2021, **118**, e2022339118.

89 A. D. Polyanin and A. V. Manzhirov, *Handbook of Mathematics for Engineers and Scientists*, Chapman & Hall, Chapman & Hall/CRC Taylor & Francis Group 6000, Broken Sound Parkway NW, Suite 300 Boca Raton, FL 33487-2742, 2007.

90 J. R. Kern and W. F. Bland, *Solid Mensuration*, John Wiley & Sons, 2nd edn, 1967.